ACS APPLIED MATERIALS & INTERFACES

Research Article

www.acsami.org

Single-Step Plasma Synthesis of Carbon-Coated Silicon Nanoparticles

Rohan P. Chaukulkar,[†] Koen de Peuter,[‡] Paul Stradins,[§] Svitlana Pylypenko,[∥] Jacob P. Bell,[⊥] Yongan Yang,[⊥] and Sumit Agarwal*[,†]

[†]Department of Chemical and Biological Engineering, Colorado School of Mines, Golden, Colorado 80401, United States

[‡]Department of Applied Physics, Eindhoven University of Technology, 5600 MB Eindhoven, The Netherlands

[§]National Center for Photovoltaics, National Renewable Energy Laboratory, Golden, Colorado 80401, United States

[∥]Department of Metallurgical and Materials Engineering, Colorado School of Mines, Golden, Colorado 80401, United States

[⊥]Department of Chemistry and Geochemistry, Colorado School of Mines, Golden, Colorado 80401, United States

Supporting Information

ABSTRACT: We have developed a novel single-step technique based on nonthermal, radio frequency (rf) plasmas to synthesize sub-10 nm, core–shell, carbon-coated crystalline Si (*c*-Si) nanoparticles (NPs) for potential application in Li^+ batteries and as fluorescent markers. Hydrogen-terminated *c*-Si NPs nucleate and grow in a SiH_4-containing, low-temperature plasma in the upstream section of a tubular quartz reactor. The *c*-Si NPs are then transported downstream by gas flow, and are coated with amorphous carbon (*a*-C) in a second C_2H_2-containing plasma. X-ray diffraction (XRD), X-ray photoelectron spectroscopy, and in situ attenuated total reflection Fourier transform infrared spectroscopy show that a thin, < 1 nm, 3C-SiC layer forms at the *c*-Si/*a*-C interface. By varying the downstream C_2H_2 plasma rf power, we can alter the nature of the *a*-C coating as well as the thickness of the interfacial 3C-SiC layer. The transmission electron microscopy (TEM) analysis is in agreement with the Si NP core size determined by Raman spectroscopy, photoluminescence spectroscopy, and XRD analysis. The size of the *c*-Si NP core, and the corresponding light emission from these NPs, was directly controlled by varying the thickness of the interfacial 3C-SiC layer. This size tunable emission thus also demonstrates the versatility of this technique for synthesizing *c*-Si NPs for potential applications in light emitting diodes, biological markers, and nanocrystal inks.

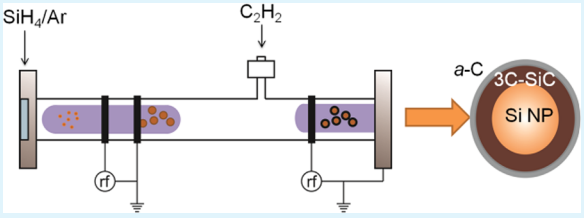

KEYWORDS: *Si nanoparticles, radio frequency plasmas, nanoparticle synthesis*

1. INTRODUCTION

Recent advances in portable electronics, mobile communication, and electric vehicles have increased the need for efficient energy storage and conversion devices.[1,2] Lithium-ion batteries (LIBs) due to their high energy and power density, high operating voltage, and low self-discharge and maintenance, are attractive candidates for energy storage.[1−5] To further improve the existing LIB technology, it is necessary to develop new materials that enable significantly higher charge capacities.[6,7] Silicon is considered one of the most promising anode materials for LIBs due to its high theoretical charge capacity (~4200 mAh/g), which is nearly ten times that for the conventional anode material, graphite (~372 mAh/g).[3,4] However, there are several challenges associated with the use of bulk Si as the anode material. Upon lithiation, Si undergoes a significant volume expansion, ~300%,[3−5] and the resulting stress leads to electrode pulverization and a subsequent loss of electrical contact between the Si fragments.[3−5] Additionally, fresh electrode surfaces, created due to pulverization of Si during continuous expansion and contraction cycles, are exposed to the electrolyte resulting in electrolyte decomposition on the Si surface, and the formation of a thick solid electrolyte interface (SEI) layer.[4,5,8,9] These factors lead to a rapid decrease in battery capacity after the first few charging and discharging cycles. In addition, since the conductivity of Li^+ in Si is low, use of bulk Si leads to an increased cycle duration.[10,11] Silicon nanostructures coated with carbon, have been proposed as a possible solution to circumvent these challenges, and numerous recent reports indicate promising results for carbon-coated Si nanostructures.[9,11,12] However, these nanostructures often require a complex synthesis route involving multiple steps.[12−14] Additionally, the critical size of the nanostructures under which crack initiation and propagation would become energetically unfavorable has not yet been accurately determined.[15,16] Recent reports suggest that sub-10 nm Si nanoparticles (NPs) may demonstrate better capacity retention.[17−19]

Previously, nonthermal plasma synthesis has been shown to be a scalable method for the synthesis of monodisperse, H-terminated, crystalline Si (*c*-Si) NPs with excellent control over their size.[20−23] Later, Coulombe and co-workers introduced a dual-plasma technique for the synthesis of surface-function-

Received: July 25, 2014
Accepted: October 2, 2014
Published: October 2, 2014

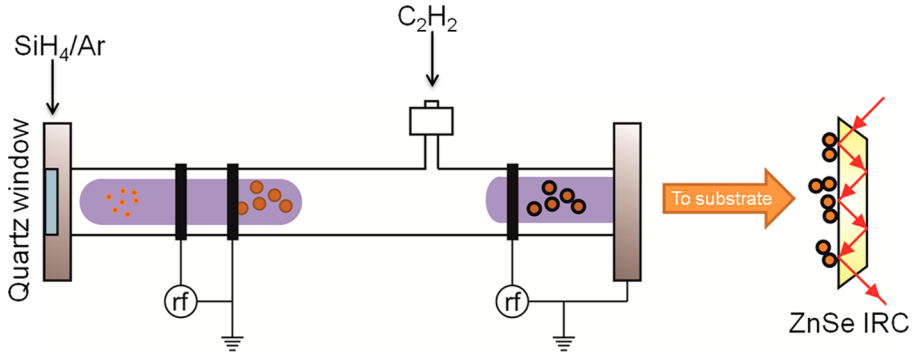

Figure 1. Schematic of the tubular reactor equipped with two radio frequency, capacitively-coupled plasma sources used to synthesize carbon-coated *c*-Si NPs. The *c*-Si NPs were synthesized in the upstream plasma using SiH_4 heavily diluted in Ar. C_2H_2 was injected into the tube beyond the afterglow region of the SiH_4/Ar plasma. The as-synthesized *c*-Si NPs were transported by gas flow to the downstream C_2H_2 plasma, where they were coated in flight with amorphous carbon and collected onto a ZnSe internal reflection crystal for characterization using surface infrared spectroscopy.

alized NPs.[24,25] In this article, we describe a single-step, nonthermal, radio frequency (rf) plasma synthesis technique for the growth of sub-10 nm, carbon-coated Si NPs using two capacitively-coupled plasmas in series. We show that the *c*-Si NPs nucleated and grew in the upstream SiH_4-containing plasma with >90% feed gas depletion. These *c*-Si NPs were coated with amorphous carbon (*a*-C) downstream in-flight in a C_2H_2-containing plasma.

2. EXPERIMENTAL DETAILS

2.1. Plasma Synthesis Setup. A schematic of the tubular quartz reactor used to synthesize the carbon-coated *c*-Si NPs is shown in Figure 1. The total length of the quartz tube between the two vacuum flanges, the external tube diameter, and the tube wall thickness were 340, 9.5, and 1 mm, respectively. The reactor was evacuated with a mechanical pump (Edwards E2M28) with a base pressure of ~6 mTorr. The two nonthermal, capacitively-coupled plasma sources were independently rf-powered at 13.56 MHz via π-type impedance matching networks. The *c*-Si NP synthesis technique was similar to the one reported previously by Kortshagen and co-workers.[20] The upstream plasma consisted of two Cu ring electrodes with an internal diameter and width of 9.5 and 10 mm, respectively. The rf-powered electrode was 50 mm from the upstream flange with the grounded electrode 30 mm further downstream from the rf-powered electrode. SiH_4 (1.4 standard cm^3/min (sccm)), heavily diluted in Ar (275 sccm), was injected upstream via mass flow controllers (see Figure 1).[22,23,26] The rf power to the upstream plasma was set at 50 W (RFVII RF-3 power supply with MN-500 matching network). Previously, we have shown that at an rf power of 50 W in the upstream plasma, the depletion of SiH_4 was ~90%.[22] C_2H_2 was injected at 300 sccms through a mass flow controller into the quartz tube, 18 cm from the upstream vacuum flange. The injection point was chosen such that it was beyond the afterglow region of the upstream SiH_4/Ar plasma. This afterglow extended ~3 cm downstream from the grounded electrode (see Figure 1). The rf-powered Cu ring electrode for the second plasma source was placed 3 cm from the downstream vacuum flange, which was also used as the grounded electrode. The rf power to the C_2H_2 plasma was over the range of 40−135 W (RFPP 5S power supply with in-house-built matching network). The pressure was measured upstream using a capacitance manometer.

2.2. Plasma and Surface Diagnostics. Optical emission spectroscopy (OES) data was recorded by sampling light through a quartz window placed upstream from the plasma (see Figure 1). The emission intensities for the Ar ($2p_1 \rightarrow 1s_2$, 750.4 nm)[27] and C_2 radical ($A^3\Pi_g \rightarrow X^3\Pi_u$, 516.5 nm)[28] lines were monitored with and without downstream C_2H_2 injection. The Si NPs were transported by gas flow into to an in-house-built surface analysis chamber equipped with an in situ attenuated total reflection Fourier transform infrared (ATR-FTIR) spectroscopy setup.[29] The Si NPs were collected at room temperature onto a 50 × 10 × 1 mm trapezoidal ZnSe internal reflection crystal (IRC) with their short edges beveled at 45°. In the ATR mode, at room temperature, ZnSe is transparent in the infrared up to ~700 cm^{-1}. Infrared data were recorded over the spectral range of 700−4000 cm^{-1} at a resolution of 4 cm^{-1} using 500 averages. All infrared spectra were recorded as difference spectra, where a reference spectrum was collected before the NPs were deposited onto the IRC. For ex situ characterization, the Si NPs were collected on to a *c*-Si(100) wafer placed adjacent to the ZnSe IRC. Photoluminescence studies were performed ex situ with excitation from a 365 nm laser diode (ThorLabs). Photoluminescence (PL) from these Si NCs was collected through a 4.5″ quartz viewport, and focused with a quartz lens into an Ocean Optics (QP1000−2-VIS-NIR) optical fiber that directed the light to a spectrometer (Si charge-coupled device, Ocean Optics) with a spectral resolution of 0.36 nm. The PL spectra were corrected for the system response by calibrating with a tungsten lamp, which was at a temperature of 3100 K. The crystallinity of the carbon-coated Si NPs was characterized using ex situ X-ray diffraction (XRD) (Philips X'Pert Pro Diffractometer, Cu Kα source), the data were recorded with a resolution of 0.05° over 2θ = 20−60°. Raman spectroscopy (Jasco NRS-3100, 532 nm laser) and transmission electron microscopy (TEM) (Philips (FEI) CM200) analysis were used to determine the size of the core of the Si NPs and the structure of the *a*-C coating. X-ray photoelectron spectroscopy (XPS) analysis of the carbon-coated *c*-Si NPs was performed (Kratos Nova) with a monochromatic Al Kα source operated at 300 W. The *c*-Si NPs were pressed onto a nonconductive adhesive tape, and during acquisition of the spectra were subject to charge compensation using low-energy electrons. Survey and high-resolution spectra of C 1s, O 1s, and Si 2p regions were acquired at pass energies of 160 and 20 eV, respectively. Data analysis was performed using the CasaXPS software, and included linear background subtraction, smoothing, charge referencing, and curve-fitting. The spectra were calibrated by setting the Au 4f peak to 84 eV. High-resolution Si 2p spectra were fitted with a series of Gaussian−Lorentzian functions. Each Si peak contains $2p_{3/2}$ and $2p_{1/2}$ components constrained to have ratio of 0.67 in area under the peak with a separation of 0.6 eV. Elemental concentrations and distribution of species in the Si 2p spectra are reported as average values, based on analysis of three different areas on a sample.

3. RESULTS AND DISCUSSION

The OES data in Figure 2 shows that injection of C_2H_2 downstream did not perturb the upstream SiH_4/Ar plasma significantly. The emission intensity of the C_2 line in the upstream plasma at 516.5 nm remained essentially unchanged suggesting minimal back diffusion of C_2H_2 or its radical fragments to the upstream *c*-Si NP synthesis plasma.

Emission from the Ar line in the upstream plasma at 750.4 nm decreased in intensity by ~10%, most likely due to the

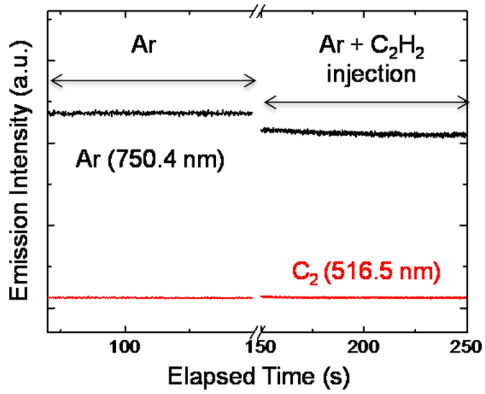

Figure 2. Optical emission spectra showing the effect of C_2H_2 injection on the upstream *c*-Si NP synthesis plasma. The emission intensities for the Ar and C_2 radical lines at 750.4 and 516.5 nm, respectively, were monitored in the upstream plasma prior to and after downstream C_2H_2 injection.

change in the upstream pressure from 5.3 to 7.3 Torr upon injection of C_2H_2 downstream. Thus, the OES data in Figure 2 confirms that the two plasma sources were operated nearly independent of each other: H-terminated *c*-Si NPs were synthesized in the upstream plasma where SiH_4 was almost completely depleted, and these NPs were coated with *a*-C in the downstream C_2H_2 plasma. The size of the Si NPs synthesized using the nonthermal plasma technique has been shown to depend on the gas pressure.[21,30] To isolate the effects of the downstream C_2H_2 plasma, all the experiments in this work were performed at constant gas flow rates while varying only the C_2H_2 plasma rf power. Figure 3 shows in situ infrared

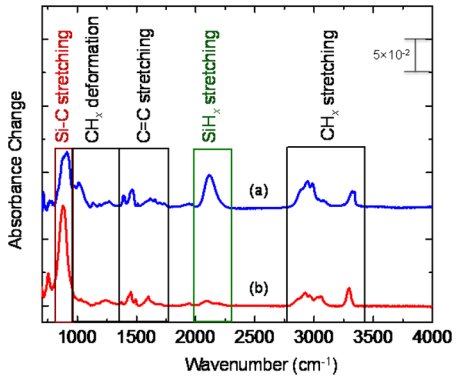

Figure 3. In situ infrared difference spectra for carbon-coated *c*-Si NPs grown at (a) 40 and (b) 90 W rf power to the downstream C_2H_2 plasma.

spectra for carbon-coated *c*-Si NPs synthesized at 40 and 90 W rf power to the downstream C_2H_2 plasma. As reported previously, the surface of SiH_4-plasma-synthesized *c*-Si NPs is terminated with SiH_x (x = 1, 2, 3) groups.[22,31] As OES indicates no back diffusion of C_2H_2 to the upstream plasma, the *c*-Si NPs synthesized in the upstream plasma are also expected to be H-terminated. These H-terminated NPs are then carbon-coated in flight when exposed to reactive hydrocarbon radicals in the downstream C_2H_2 rf plasma. In addition to C_2H_2 gas, the downstream plasma contained Ar and a small fraction of SiH_4, which was injected upstream. When the C_2H_2 plasma was operated at 40 W rf power, the infrared spectrum (see Figure 3, spectrum "a") shows a strong absorption band centered at ~2100 cm^{-1}, which was assigned to the SiH_x (x = 1, 2, 3) stretching mode.[22] This indicates that the surface of the *c*-Si NPs after carbon coating was still predominantly H-terminated. In addition, we also observed an increase in absorbance in the 750−950, 950−1400, 1400−1700, and 2800−3400 cm^{-1} regions, which have been assigned to the SiC stretching mode, CH_x deformation modes, C═C stretching modes, and CH_x stretching modes, respectively.[26,32−39] The presence of various C-containing species detected by infrared spectroscopy clearly suggests the formation of an *a*-C coating around the *c*-Si NPs in the downstream C_2H_2 plasma.[40−42] The CH_x stretching modes in the 2800−3400 cm^{-1} region were further categorized based on the hybridization of the C atom. The vibrational modes in the 2800−2980 and 2980−3100 cm^{-1} region were assigned to the sp^3-and sp^2-hybridized CH_x species, respectively.[26,38,39,41,43] The CH_x stretching modes in the 3000−3100 cm^{-1} region were assigned to the aromatic sp^2-hybridized species, which indicates the formation of aromatic ring structures in the *a*-C coating around *c*-Si NPs.[26,38,43] The peak centered at ~3300 cm^{-1} was assigned to the CH stretching mode for sp-hybridized species indicating alkenyl termination of the surface of *c*-Si NPs, in addition to the SiH_x groups.[39,44] In addition, the SiC stretching vibration in the 750−950 cm^{-1} region was attributed to the transverse optical (TO) phonon mode of SiC.[32,33,35,36] Thus, the infrared spectrum in Figure 3 (spectrum "a") suggests that SiC is formed at the *c*-Si/*a*-C interface due to the reaction of hydrocarbon radicals with the H-terminated *c*-Si surface.

When the downstream C_2H_2 plasma was operated at higher rf power, 90 W, (see Figure 3, spectrum "b"), we observed almost no absorption in the SiH_x stretching region at ~2100 cm^{-1} as compared to a strong absorption band in the 750−950 cm^{-1} region corresponding to the Si—C stretching mode in SiC. At higher rf power to the C_2H_2 plasma, the hydrocarbon radical density and the NP temperature are expected to be higher.[20,45] The reaction of these hydrocarbon radicals with the surface of *c*-Si NPs resulted in the formation of a significant amount of SiC on the NP surface at the *c*-Si/*a*-C interface, and almost complete consumption of surface SiH_x (x = 1, 2, 3) species. This SiC is not expected to be on the outermost surface since SiH_4 is almost completely depleted in the upstream region, and the flow rate of C_2H_2 (300 sccm) into the downstream plasma is more than 3 orders of magnitude greater the undepleted SiH_4 (~10% of 1.4 sccm). In addition, in spectrum "b" in Figure 3, we also observed a change in the shape and relative intensities of the different CH_x and C═C stretching regions as compared to spectrum "a" in Figure 3: this clearly indicates that changing the downstream plasma rf power from 40 to 90 W also affected the H-content and the sp^2/sp^3 hybridization ratio of the C atoms in the *a*-C coating. To study this effect of plasma power on the type of *a*-C layer deposited, we deconvoluted the CH_x stretching region for carbon-coated *c*-Si NPs synthesized at three different downstream plasma rf powers − 40, 60, and 90 W (see Figure 4). Deconvolution of the infrared spectra based on peak assignments in the literature enabled us to determine the relative changes in the concentration of the various hybridization states of the C atoms present in the *a*-C network. The infrared spectra were deconvoluted using four Gaussian line-shapes with peaks centered at ~2880, ~2930, ~2970, and ~3050 cm^{-1}. The peaks centered at ~2880 and ~2970 cm^{-1} were assigned to symmetric and antisymmetric stretching modes of CH_3, while the peak at ~2930 cm^{-1} was assigned to the symmetric

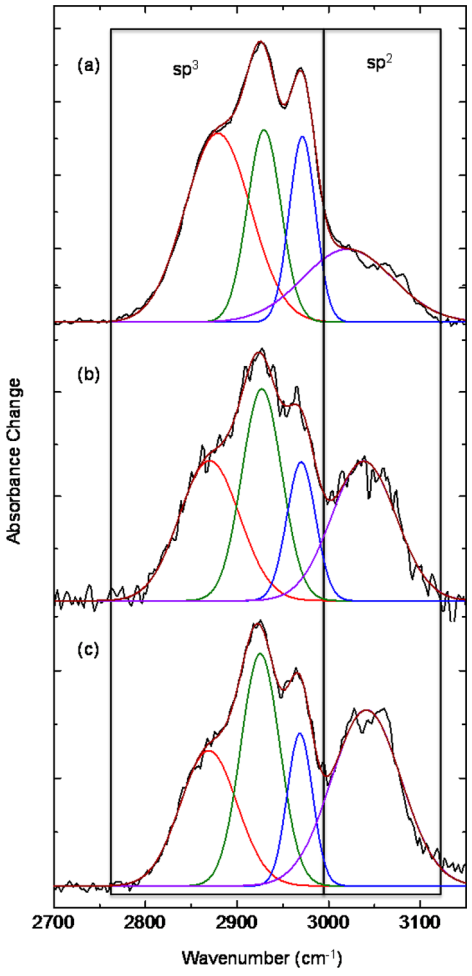

Figure 4. Infrared difference spectra showing the CH_x stretching region for carbon-coated *c*-Si NPs synthesized at (a) 40 W, (b) 60 W, and (c) 90 W rf power to the downstream C_2H_2 plasma. The spectra were deconvoluted with four Gaussian line shapes. The ratio of the integrated absorbance of the sp^2-hybridized carbon to that of the sp^3-hybridized carbon increased with increasing downstream plasma rf power.

stretching mode of sp^3-hybridized CH_2.[26,38,39,41,43,44] The peak at ~3050 cm^{-1} was assigned to the stretching mode for sp^2-hybridized CH.[26,43] The integrated absorbance for each of the deconvoluted vibrational modes (see Figure 4) is directly proportional to corresponding bond density and its infrared absorption cross section.[23,26] Since the infrared absorption cross section of various CH stretching vibrations in *a*-C are not reported in the literature, we estimated the sp^2-to-sp^3 hybridized C ratio in the *a*-C network by taking the ratio of total integrated absorbances of the sp^2 and sp^3 hybridized CH_x species. This ratio was 0.27, 0.43, and 0.60 at 40, 60, and 90 W, respectively, clearly indicating that the fraction of graphitic or aromatic sp^2-hybridized C content increased with the downstream plasma power, regardless of the infrared absorption cross section of the individual bands. According to previous reports in literature, the sp^2 content of *a*-C films was shown to increase upon thermal annealing due to the atomic H desorption from the sp^3-hybridized C atoms, and subsequent local restructuring to sp^2-hybridized C.[46−49] In our experiments, this observation can be explained based on the plasma-induced heating of the carbon-coated *c*-Si NPs due to the exothermic ion-electron and neutral-neutral recombination reactions that occur on the NP surface in a plasma environment.[20,22,45] Previous reports suggest that these exothermic reactions result in Si NP heating to temperatures that are sufficiently high for crystallization (>800 K) given that their melting point is significantly reduced compared to bulk *c*-Si.[45] The maximum temperature of the NPs in the plasma depends on the applied rf power.[20,22,45] Previously, we showed that heating of Si NPs in the plasma not only affects their crystallinity, but also affects the surface SiH_x (x = 1,2,3) composition, as the population of higher hydrides decreases due to their lower thermal stability.[22] Similarly, as the downstream C_2H_2 plasma rf power is increased, the core−shell NPs reach higher temperatures,[20,22,45] which leads to H-desorption from sp^3 C and thus a higher sp^2 C content in the *a*-C network.

Our previous studies show that the PL emission energy from these *c*-Si NPs is consistent with quantum confinement effects, which results in a NP-size-dependent band gap.[22] Thus, the emission energy can be used to estimate the average size of the *c*-Si NPs.[50−52] Figure 5 shows normalized PL spectra for *c*-Si

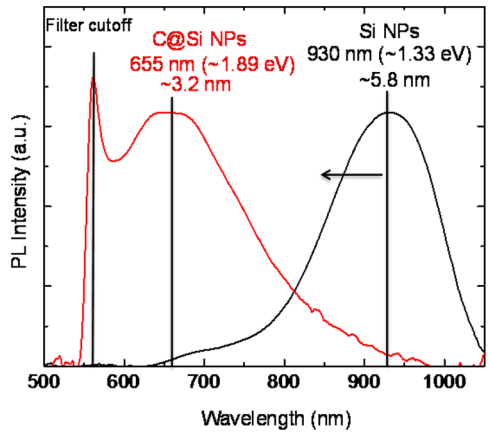

Figure 5. Normalized PL spectra for uncoated (black) and carbon-coated (red) *c*-Si NPs. The carbon coating was accompanied by the formation of a 3C-SiC at the *c*-Si/*a*-C interface, which led to the consumption of surface Si, and a reduction in the size of the NP core. In the quantum confinement regime, this causes a blue-shift in the PL peak position.

NPs synthesized with the downstream C_2H_2 plasma turned off, and carbon-coated *c*-Si NPs synthesized with the downstream C_2H_2 plasma operated at 90 W rf power. Since in both experiments the upstream NP synthesis conditions were identical, we attribute the blueshift from 930 nm for the primarily H-terminated *c*-Si NPs to 655 nm for carbon-coated *c*-Si NPs to the consumption of the Si core due to reaction with *a*-C to form SiC: this is also consistent with the infrared data in Figure 3, which shows infrared absorption due to the Si—C stretching vibrations.

Using accepted quantum confinement models for *c*-Si, this blueshift in emission corresponds to a reduction in the Si core size from ~5.8 to ~3.2 nm.[50] Additionally, when the downstream C_2H_2 plasma was operated at the lowest rf power (40 W), we observed an absorbance band due to stretching vibrations of surface SiH_x (x = 1,2,3) (Figure 3, spectrum (a)) species suggesting all surface Si atoms in the core were not bonded to C atoms in the coating. However, when the C_2H_2 plasma power was increased to 90 W, almost all the surface SiH_x (x = 1,2,3) species were consumed indicating a

denser shell structure (Figure 3, spectrum (a)). This suggests the C_2H_2 plasma has to be operated at high powers to ensure a dense coating. Hence, to determine the effect of the C_2H_2 plasma rf power on the carbon-coated Si NPs, all further characterization results presented below are for C_2H_2 plasma rf powers between 90 and 135 W.

To determine the structure of the interfacial SiC layer, we performed XRD analysis on Si NPs that were synthesized at different rf powers for downstream plasma, but otherwise identical process conditions. The diffractograms in Figure 6

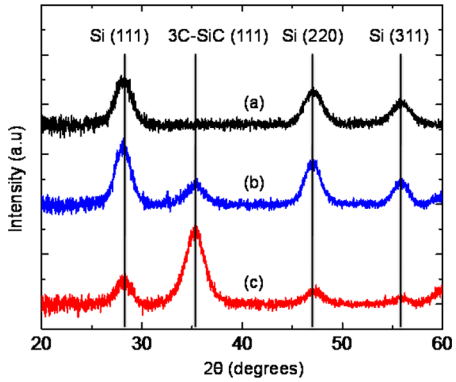

Figure 6. XRD patterns for the *c*-Si NPs grown at (a) 0, (b) 105, and (c) 135 W rf power to the downstream C_2H_2 plasma, but identical upstream plasma conditions. As the C_2H_2 plasma rf power was increased, the amount of 3C-SiC formed at the *c*-Si/*a*-C interface increased, which is indicated by the increase in the relative intensity of the 3C-SiC (111) diffraction peak compared to the Si (111) diffraction peak.

show that when the rf power to the downstream plasma was turned off, diffraction peaks appeared corresponding to the (111), (220), and (311) crystallographic planes of Si indicating the presence of *c*-Si NPs.[22] At 105 W rf power to the downstream C_2H_2 plasma (pattern (b)), we also observed an additional diffraction peak at $2\theta \approx 36°$, which corresponds to the (111) crystallographic plane of 3C-SiC.[53,54] Diffraction peaks corresponding to other crystallographic planes of 3C-SiC lie outside the range of measurements in Figure 6. The presence of the 3C-SiC(111) peak in pattern "b" in Figure 6 clearly suggests that a crystalline SiC layer forms at the *c*-Si/*a*-C interface in the downstream C_2H_2 plasma due to carburization of surface Si atoms in the Si NPs. When the downstream C_2H_2 plasma rf power was further increased to 135 W (see pattern (c)), we observed an increase in intensity for the 3C-SiC(111) peak as compared to the Si(111) peak showing that the extent of carburization of surface Si atoms increases at higher rf power to the C_2H_2 plasma: we attribute this increase in surface carburization to a higher NP temperature[20,45] combined with a higher flux of hydrocarbon radicals to the NP surface. In multicomponent mixtures, the integrated intensity of an XRD peak for a particular component depends upon its volume fraction in the mixture, the crystal structure parameters of the phase such as the structure and the multiplicity factors, and the linear absorption coefficient of the phase.[54] Therefore, by comparing the integrated intensities of the (111) peaks for Si and 3C-SiC we can quantitatively estimate the volume fractions of the two phases in the mixture using the expression in eq 1.

$$\frac{I_{Si}(111)}{I_{SiC}(111)} = \left(\frac{|F_{Si}(111)|^2}{|F_{SiC}(111)|^2}\right)\left(\frac{L_{Si}}{L_{SiC}}\right)\frac{\mu_{SiC}v_{SiC}^2V_{Si}}{\mu_{Si}v_{Si}^2V_{SiC}} \quad (1)$$

In eq 1 above, I is the integrated intensity of the diffraction peak, F is the structure factor, L is the Lorentz polarization factor, v is the volume of the unit cell, V is the volume fraction, and μ is the linear absorption coefficient. The subscripts in eq 1 indicate the crystalline material, and the parentheses contain the Miller indices for the crystallographic plane. The linear absorption coefficient for 3C-SiC, μ_{SiC}, was calculated based on the linear absorption coefficients of Si and C and their respective weight fractions in 3C-SiC according to eq 2 below,[54]

$$\left(\frac{\mu_{SiC}}{\rho_{SiC}}\right) = w_{Si}\left(\frac{\mu_{Si}}{\rho_{Si}}\right) + w_C\left(\frac{\mu_C}{\rho_C}\right) \quad (2)$$

where, w is the weight fraction of Si or C in SiC, and ρ is the density. Thus, the expressions in eq 1 and 2, with μ_{Si}/ρ_{Si} = 65.32 cm^2/g and μ_C/ρ_C = 4.219 cm^2/g for Cu $K\alpha$ radiation,[54] can be used to determine the volume ratio of Si and 3C-SiC.

When the downstream C_2H_2 plasma rf power was turned off, using PL measurements (see Figure 5), the average size of the *c*-Si NPs was estimated to be ~5.8 nm. As the two plasmas operate practically independent of each other, changing the downstream C_2H_2 plasma rf power would not affect the size of the *c*-Si NPs synthesized in the upstream plasma. Hence, the change in size of the *c*-Si NPs is almost entirely due to formation of the 3C-SiC shell in the downstream C_2H_2 plasma. Therefore, by calculating the volume fractions of the *c*-Si and 3C-SiC from the XRD patterns (see eqs 1 and 2), we can estimate the size of the *c*-Si core and the thickness of the 3C-SiC shell. The quantitative XRD analysis shows that as the downstream C_2H_2 plasma rf power increased, the volume fraction of 3C-SiC also increased, which led to a decrease in the size of the *c*-Si core of the NPs. For the *c*-Si NPs synthesized at C_2H_2 plasma rf powers of 105 and 135 W, we estimated the ~5.8 nm-diameter *c*-Si core was reduced to ~4.6 and 3.5 nm, respectively, due to carburization which results in a 3C-SiC layer of ~0.5 and 0.7 nm, respectively.

The 3C-SiC interlayer was formed by the reaction between the *a*-C coating and the *c*-Si NP core. On the basis of previous work by Mangolini and Kortshagen,[55] an increase in the C_2H_2/Ar plasma rf power is expected to lead to an increase in the average temperature and the magnitude of the temperature fluctuation of these carbon-coated *c*-Si NPs in the downstream plasma. As the NP temperature increases, we expect that the extent of carburization of the *c*-Si NP core increases due to enhanced diffusion of the C atoms from the outer *a*-C coating, through the intermediate 3C-SiC layer, into the *c*-Si core.

The *c*-Si NPs synthesized at 135 W C_2H_2 plasma rf power were further characterized via Raman spectroscopy (see Figure 7(a)). The Raman-active transverse optical phonon mode for bulk *c*-Si is at 521 cm^{-1}, which red-shifts in *c*-Si nanostructures due to phonon confinement.[56−58] Therefore, the position of the Raman band in nanostructured *c*-Si provides an estimate of the average size of the nanocrystals. The Raman spectrum in Figure 7(a) was deconvoluted over the 300−600 cm^{-1} region using a Lorentzian line shape for *c*-Si centered at ~510 cm^{-1} and a Gaussian line shape centered at ~450 cm^{-1} (see Figure 7(b)).

The red-shift in the *c*-Si phonon band from 521 to 510 cm^{-1} corresponds to *c*-Si NPs with an average core size of ~3.5

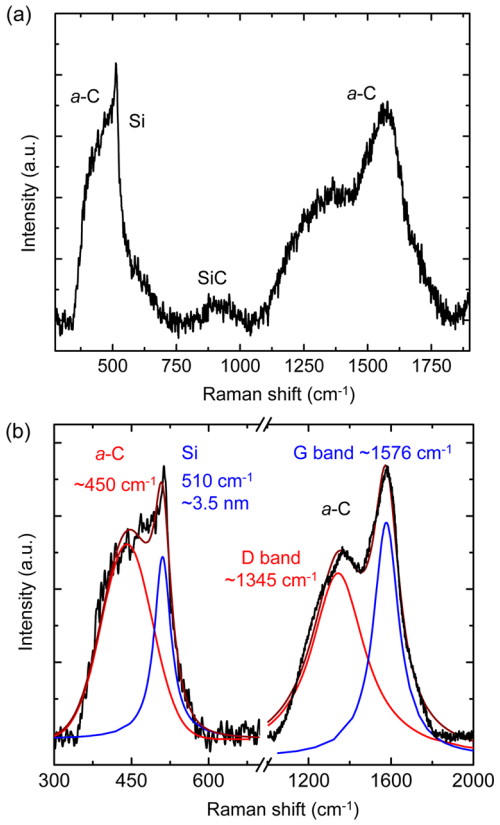

Figure 7. (a) Raman spectrum showing the presence of *c*-Si NPs, *a*-C, and 3C-SiC for carbon-coated *c*-Si NPs grown at 135 W rf power to the C_2H_2 plasma. (b) The *c*-Si region was fit using a Lorentzian line shape centered at 510 cm^{-1}, while the shoulder attributed to *a*-C, was fit with a Gaussian line shape centered at ∼450 cm^{-1}. The *a*-C region was fit with a Lorentzian centered at ∼1345 cm^{-1} (D band), and a Breit−Wigner−Fano line shape centered at ∼1576 cm^{-1} (G band).

nm.[57,58] The peak at ∼450 cm^{-1} was attributed to the bending modes of the sp-hybridized C present in the outermost *a*-C coating around the *c*-Si NPs.[59] Additionally, the Raman spectrum also contains a distinct band over the 1100−2000 cm^{-1} region (see Figure 7 (a)), which was deconvoluted using two Gaussian line shapes centered at ∼1576 and ∼1345 cm^{-1} assigned to the G and D bands of *a*-C (see Figure 7(b)).[60,61]

The G peak in the Raman spectrum for *a*-C is observed due to the sp^2 stretching vibrations of the aromatic or olefinic chain structures, while the D peak arises due to structural disorder, and requires the presence of six-membered aromatic rings.[60] Thus, the presence of the D band in the Raman spectrum confirms the presence of a graphitic fraction in the *a*-C coating. Finally, in the Raman spectrum in Figure 7(a), we also observed a band at ∼940 cm^{-1}, which was assigned to the longitudinal optical phonon mode of 3C-SiC.[53] Thus, for the case of *c*-Si/*a*-C core−shell NPs synthesized at 135 W rf power to the C_2H_2 plasma, the *c*-Si core size determined from the Raman analysis (∼3.5 nm) agrees well with the size obtained from the PL (∼3.2 nm) and XRD (∼3.5 nm) analysis. Figure 8(a) shows a TEM image of the *c*-Si NPs synthesized at C_2H_2 plasma power of 135 W. A zoomed-in view of image (a) is shown in image (b), which clearly shows a c-Si NP with a ∼3.7 nm core with a ∼1.5 nm coating. Thus, TEM analysis further confirms the size of the NPs as determined by Raman spectroscopy and XRD analysis. In Figure 8(b), no lattice fringes were observed for 3C-SiC most likely due to the

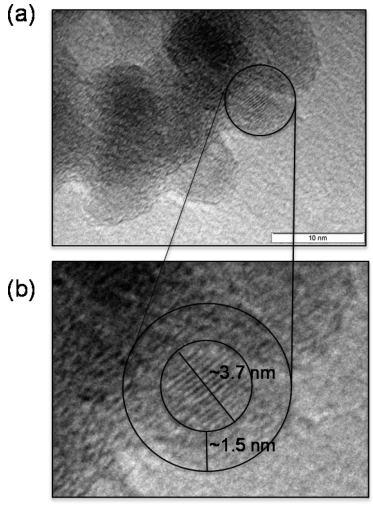

Figure 8. TEM images of carbon-coated *c*-Si NPs grown at 135 W rf power to the downstream C_2H_2 plasma. Image (b), which is a zoomed-in view of a particle that was observed in image (a), clearly shows a *c*-Si core of ∼3.7 nm with a ∼1.5 nm-thick coating.

different low-index zone axis alignment of the core and shell crystal structures, combined with the fact that the 3C-SiC is coating very thin. The quantitative XRD analysis combined with the TEM image analysis further allows us to estimate the composition of the coating around the *c*-Si core. In this particular experiment, from the XRD analysis we estimated that the thickness of the interfacial 3C-SiC layer was ∼0.7 nm, which implies that the rest of the ∼0.8 nm thick coating is the *a*-C film.

The elemental and chemical composition of the *c*-Si NPs was also obtained using XPS analysis. Since the size of the carbon-coated *c*-Si NPs is comparable to the escape depth of photoelectrons (∼2−5 nm),[62] XPS analysis is not limited to just the surface of the NPs, but provides an estimate of the bulk composition. Given that the XPS analysis was performed ex situ, the surface of the *c*-Si NPs undergoes some degree of oxidation along with physisorption of hydrocarbons. Therefore, the carbon-coated *c*-Si NPs synthesized at 135 W rf power to the downstream C_2H_2 plasma show ∼45 at. % C, 35 at. % Si, and 20 at. % O. A corresponding representative high-resolution Si 2p spectrum is shown in Figure 9, which was fitted with 4 sets of Gaussian−Lorentzian peaks, each consisting of two

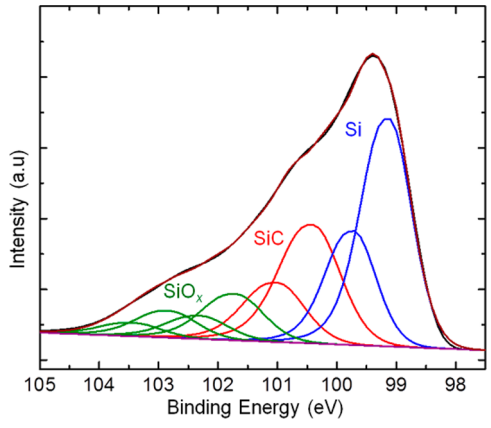

Figure 9. High resolution XPS scan of the Si 2p region for carbon-coated *c*-Si NPs synthesized at 135 W rf power to the C_2H_2 plasma.

dx.doi.org/10.1021/am504913n | ACS Appl. Mater. Interfaces 2014, 6, 19026−19034

components, $2p_{3/2}$ and $2p_{1/2}$, separated by 0.6 eV. The $2p_{3/2}$ component of the first doublet is centered at 99.2 ± 0.1 eV and attributed to elemental Si.[63,64] The second $2p_{3/2}$ component centered at 100.5 ± 0.1 eV, and is due to SiC.[65,66] Doublets with $2p_{3/2}$ components located at 101.9 and 102.8 eV are due to various SiO_x species.[67−69] On the basis of these peak assignments, Si was present in these carbon-coated *c*-Si NPs primarily as elemental Si and SiC, with their respective concentrations of 45 ± 5% and 38.5 ± 7%, while the rest of the Si (∼16.5 ± 2%) is bound to oxygen.

4. CONCLUSIONS

We have developed a single-step process to synthesize *a*-C-coated Si NPs < 10 nm in size using a dual-plasma setup. We have demonstrated that the sp^2-to-sp^3 hybridization ratio of the *a*-C coating as well as the thickness of the interfacial 3C-SiC layer can be manipulated through the downstream C_2H_2 plasma rf power, which in turn controls the hydrocarbon radical flux and plasma-induced heating of the NPs. The 3C-SiC layer has direct implications for the use of these NPs in LIBs. While 3C-SiC conducts Li ions, it does not undergo lithiation. Therefore, this interfacial layer does not contribute to the lithiation capacity of the *a*-C-coated Si NPs thereby reducing the effective charge capacity of the LIBs.[70] Hence, the downstream C_2H_2 plasma should be operated under conditions which result in a high graphitic content in the *a*-C coating while minimizing the amount of 3C-SiC formed. Given that the size of the *c*-Si NP core and the light emission wavelength (see Figure 5) were directly controlled by varying the thickness of the interfacial 3C-SiC layer, we have demonstrated that this technique can be also used for synthesizing *c*-Si NPs for potential applications in light emitting diodes, biological markers, and nanocrystal inks.

■ ASSOCIATED CONTENT

Supporting Information

Detailed procedure for quantitative XRD analysis. This material is available free of charge via the Internet at http://pubs.acs.org.

■ AUTHOR INFORMATION

Corresponding Author

*E-mail: sagarwal@mines.edu.

Author Contributions

The manuscript was written through contributions of all authors. All authors have given approval to the final version of the manuscript.

Notes

The authors declare no competing financial interest.

■ ACKNOWLEDGMENTS

We gratefully acknowledge support from the NSF CAREER program (Grant No. CBET-0846923). P.S. acknowledges support from U.S. Department of Energy under Contract No. DE-AC36-08-GO28308 with the National Renewable Energy Laboratory. K.d.P. acknowledges support from the Eindhoven University of Technology. The authors would like to thank H. A. MacPherson and Dr. C. R. Stoldt at the University of Colorado for the Raman measurements, and the surface analysis group at the National Renewable Energy Laboratory for support and access to the XPS.

■ REFERENCES

(1) Armand, M.; Tarascon, J.-M. Building Better Batteries. *Nature* **2008**, *451*, 652−657.

(2) Tarascon, J.-M.; Armand, M. Issues and challenges facing rechargeable lithium batteries. *Nature* **2001**, *414*, 359−367.

(3) Gu, M.; Li, Y.; Li, X.; Hu, S.; Zhang, X.; Xu, W.; Thevuthasan, S.; Baer, D. R.; Zhang, J.-G.; Liu, J.; Wang, C. In situ TEM study of Lithiation Behavior of Silicon Nanoparticles Attached to and Embedded in a Carbon Matrix. *ACS Nano* **2012**, *6*, 8439−8447.

(4) Liu, B.; Soares, P.; Checkles, C.; Zhao, Y.; Yu, G. Three-Dimensional Hierarchical Ternary Nanostructures for High-Performance Li-Ion Battery Anodes. *Nano Lett.* **2013**, *13*, 3414−3419.

(5) Wu, H.; Cui, Y. Designing Nanostructured Si Anodes for High Energy Lithium Ion Batteries. *Nano Today* **2012**, *7*, 414−429.

(6) Graetz, J.; Ahn, C. C.; Yazami, R.; Fultz, B. Highly Reversible Lithium Storage in Nanostructured Silicon. *Electrochem. Solid-State Lett.* **2003**, *6*, A194−A197.

(7) Hu, Y.-S.; Demir-Cakan, R.; Titirici, M.-M.; Müller, J.-O.; Schlögl, R.; Antonietti, M.; Maier, J. Superior Storage Performance of a Si@SiO_x/C Nanocomposite as Anode Material for Lithium-ion Batteries. *Angew. Chem., Int. Ed. Engl.* **2008**, *47*, 1645−1649.

(8) Park, M.-H.; Kim, M. G.; Joo, J.; Kim, K.; Kim, J.; Ahn, S.; Cui, Y.; Cho, J. Silicon Nanotube Battery Anodes. *Nano Lett.* **2009**, *9*, 3844−3847.

(9) Yoshio, M.; Wang, H.; Fukuda, K.; Umeno, T.; Dimov, N.; Ogumi, Z. Carbon-Coated Si as a Lithium-Ion Battery Anode Material. *J. Electrochem. Soc.* **2002**, *149*, A1598−A1603.

(10) Liu, W.-R.; Guo, Z.-Z.; Young, W.-S.; Shieh, D.-T.; Wu, H.-C.; Yang, M.-H.; Wu, N.-L. Effect of Electrode Structure on Performance of Si Anode in Li-ion Batteries: Si particle Size and Conductive Additive. *J. Power Sources* **2005**, *140*, 139−144.

(11) Cui, L.; Ruffo, R.; Chan, C.; Peng, H.; Cui, Y. Crystalline-Amorphous Core−Shell Silicon Nanowires for High Capacity and High Current Battery Electrodes. *Nano Lett.* **2008**, *9*, 491−495.

(12) Ng, S.-H.; Wang, J.; Wexler, D.; Konstantinov, K.; Guo, Z.-P.; Liu, H.-K. Highly Reversible Lithium Storage in Spheroidal Carbon-Coated Silicon Nanocomposites as Anodes for Lithium-Ion Batteries. *Angew. Chem., Int. Ed. Engl.* **2006**, *45*, 6896−6899.

(13) Li, X.; Meduri, P.; Chen, X.; Qi, W.; Engelhard, M. H.; Xu, W.; Ding, F.; Xiao, J.; Wang, W.; Wang, C.; Zhang, J.-G.; Liu, J. Hollow Core−Shell Structured Porous Si−C Nanocomposites for Li-Ion Battery Anodes. *J. Mater. Chem.* **2012**, *22*, 11014−11017.

(14) Liu, N.; Wu, H.; McDowell, M. T.; Yao, Y.; Wang, C.; Cui, Y. A Yolk-Shell Design for Stabilized and Scalable Li-Ion Battery Alloy Anodes. *Nano Lett.* **2012**, *12*, 3315−3321.

(15) Ma, Z.; Li, T.; Huang, Y.; Liu, J.; Zhou, Y.; Xue, D. Critical Silicon-Anode Size for Averting Lithiation-Induced Mechanical Failure of Lithium-Ion Batteries. *RSC Adv.* **2013**, *3*, 7398−7402.

(16) Aifantis, K. E.; Hackney, S. A.; Dempsey, J. P. Design Criteria for Nanostructured Li-Ion Batteries. *J. Power Sources* **2007**, *165*, 874−879.

(17) Kim, H.; Seo, M.; Park, M.-H.; Cho, J. A Critical Size of Silicon Nano-Anodes for Lithium Rechargeable Batteries. *Angew. Chem., Int. Ed. Engl.* **2010**, *49*, 2146−2149.

(18) Kim, C.; Noh, M.; Choi, M.; Cho, J.; Park, B. Critical Size of a Nano SnO_2 Electrode for Li-Secondary Battery. *Chem. Mater.* **2005**, *17*, 3297−3301.

(19) Xu, Y.; Liu, Q.; Zhu, Y.; Liu, Y.; Langrock, A.; Zachariah, M. R.; Wang, C. Uniform Nano-Sn/C Composite Anodes for Lithium Ion Batteries. *Nano Lett.* **2013**, *13*, 470−474.

(20) Mangolini, L.; Thimsen, E.; Kortshagen, U. High-Yield Plasma Synthesis of Luminescent Silicon Nanocrystals. *Nano Lett.* **2005**, *5*, 655−659.

(21) Kortshagen, U. Nonthermal Plasma Synthesis of Semiconductor Nanocrystals. *J. Phys. D. Appl. Phys.* **2009**, *42*, 113001−1−22.

(22) Jariwala, B. N.; Kramer, N. J.; Petcu, M. C.; Bobela, D. C.; van de Sanden, M. C. M.; Stradins, P.; Ciobanu, C. V.; Agarwal, S. Surface Hydride Composition of Plasma-Synthesized Si Nanoparticles. *J. Phys. Chem. C* **2011**, *115*, 20375−20379.

(23) Weeks, S. L.; Macco, B.; van de Sanden, M. C. M.; Agarwal, S. Gas-Phase Hydrosilylation of Plasma-Synthesized Silicon Nanocrystals with Short- and Long-Chain Alkynes. *Langmuir* **2012**, *28*, 17295−17301.
(24) Swanson, E. J.; Tavares, J.; Coulombe, S. Improved Dual-Plasma Process for the Synthesis of Coated or Functionalized Metal Nanoparticles. *IEEE Trans. Plasma Sci.* **2008**, *36*, 886−887.
(25) Qin, C.; Coulombe, S. Organic Layer-coated Metal Nanoparticles Prepared by a Combined Arc Evaporation/Condensation and Plasma Polymerization process. *Plasma Sources Sci. Technol.* **2007**, *16*, 240−249.
(26) Jariwala, B. N.; Dewey, O. S.; Stradins, P.; Ciobanu, C. V.; Agarwal, S. In Situ Gas-Phase Hydrosilylation of Plasma-Synthesized Silicon Nanocrystals. *ACS Appl. Mater. Interfaces* **2011**, *3*, 3033−3041.
(27) Crintea, D. L.; Czarnetzki, U.; Iordanova, S.; Koleva, I.; Luggenhölscher, D. Plasma Diagnostics by Optical Emission Spectroscopy on Argon and Comparison with Thomson Scattering. *J. Phys. D. Appl. Phys.* **2009**, *42*, 045208−1−11.
(28) Lin, Y. Y.; Wei, H. W.; Leou, K. C.; Lin, H.; Tung, C. H.; Wei, M. T.; Lin, C.; Tsai, C. H. Experimental Characterization of an Inductively Coupled Acetylene/Hydrogen Plasma for Carbon Nanofiber Synthesis. *J. Vac. Sci. Technol. B* **2006**, *24*, 97−103.
(29) Rai, V. R.; Agarwal, S. In Situ Diagnostics for Studying Gas-Surface Reactions during Thermal and Plasma-Assisted Atomic Layer Deposition. *J. Vac. Sci. Technol. A* **2012**, *30*, 01A158−1−10.
(30) Gresback, R.; Holman, Z.; Kortshagen, U. Nonthermal Plasma Synthesis of Size-Controlled, Monodisperse, Freestanding Germanium Nanocrystals. *Appl. Phys. Lett.* **2007**, *91*, 093119−1−3.
(31) Mangolini, L.; Kortshagen, U. Plasma-Assisted Synthesis of Silicon Nanocrystal Inks. *Adv. Mater.* **2007**, *19*, 2513−2519.
(32) Basa, D.; Smith, F. Annealing and Crystallization Processes in a Hydrogenated Amorphous Si−C Alloy Film. *Thin Solid Films* **1990**, *192*, 121−133.
(33) Choi, W. K.; Chan, Y. M.; Ling, C. H.; Lee, Y.; Gopalakrishnan, R.; Tan, K. L. Structural Properties of Amorphous Silicon Carbide Films by Plasma-Enhanced Chemical Vapor Deposition. *J. Appl. Phys.* **1995**, *77*, 827−832.
(34) Choi, W. K.; Loo, F. L.; Loh, F. C.; Tan, K. L. Effects of Hydrogen and rf Power on the Structural and Electrical Properties of rf Sputtered Hydrogenated Amorphous Silicon Carbide Films. *J. Appl. Phys.* **1996**, *80*, 1611−1616.
(35) Spitzer, W.; Kleinman, D.; Frosch, C. Infrared Properties of Cubic Silicon Carbide Films. *Phys. Rev.* **1959**, *113*, 133−137.
(36) McKenzie, D. Infrared Absorption and Bonding in Amorphous Hydrogenated Silicon-Carbon Alloys. *J. Phys. D. Appl. Phys.* **1985**, *18*, 1935−1948.
(37) Song, D.; Cho, E.-C.; Conibeer, G.; Cho, Y.-H.; Huang, Y.; Huang, S.; Flynn, C.; Green, M. A. Fabrication and Characterization of Si Nanocrystals in SiC Matrix Produced by Magnetron Cosputtering. *J. Vac. Sci. Technol. B* **2007**, *25*, 1327−1335.
(38) Grill, A.; Patel, V. Characterization of Diamondlike Carbon by Infrared Spectroscopy? *Appl. Phys. Lett.* **1992**, *60*, 2089−2091.
(39) Socrates, G. Infrared and Raman Characteristic Group Frequencies. *Infrared and Raman Characteristic Group Frequencies*; John Wiley & Sons Ltd., West Sussex, England, 2001.
(40) Louh, S. P.; Wong, C. H.; Hon, M. H. Effects of Acetylene on Property of Plasma Amorphous Carbon Films. *Thin Solid Films* **2006**, *498*, 235−239.
(41) Jariwala, B. N.; Ciobanu, C. V.; Agarwal, S. Atomic Hydrogen Interactions with Amorphous Carbon Thin Films. *J. Appl. Phys.* **2009**, *106*, 073305−1−9.
(42) Chu, P. K.; Li, L. Characterization of Amorphous and Nanocrystalline Carbon Films. *Mater. Chem. Phys.* **2006**, *96*, 253−277.
(43) McKenzie, D.; McPhedran, R.; Savvides, N.; Cockayne, D. Analysis of Films Prepared by Plasma Polymerization of Acetylene in a DC Magnetron. *Thin Solid Films* **1983**, *108*, 247−256.
(44) Huang, C.; Widdra, W.; Wang, X. S.; Weinberg, W. H. Adsorption of Acetylene on the Si(100)-(2 × 1) Surface. *J. Vac. Sci. Technol. A* **1993**, *11*, 2250−2254.
(45) Kramer, N. J.; Anthony, R. J.; Mamunuru, M.; Aydil, E. S.; Kortshagen, U. R. Plasma-induced Crystallization of Silicon Nanoparticles. *J. Phys. D. Appl. Phys.* **2014**, *47*, 075202.
(46) Nadler, M.; Donovan, T.; Green, A. Thermal Annealing Study of Carbon Films Formed by the Plasma Decomposition of Hydrocarbons. *Thin Solid Films* **1984**, *116*, 241−247.
(47) Ferrari, A. C.; Kleinsorge, B.; Morrison, N. A.; Hart, A.; Stolojan, V.; Robertson, J. Stress Reduction and Bond Stability During Thermal Annealing of Tetrahedral Amorphous Carbon. *J. Appl. Phys.* **1999**, *85*, 7191−7197.
(48) Takabayashi, S.; Okamoto, K.; Sakaue, H.; Takahagi, T.; Shimada, K.; Nakatani, T. Annealing Effect on the Chemical Structure of Diamondlike Carbon. *J. Appl. Phys.* **2008**, *104*, 043512.
(49) Mangolini, F.; Rose, F.; Hilbert, J.; Carpick, R. W. Thermally Induced Evolution of Hydrogenated Amorphous Carbon. *Appl. Phys. Lett.* **2013**, *103*, 161605.
(50) Ledoux, G.; Guillois, O.; Porterat, D.; Reynaud, C.; Huisken, F.; Kohn, B.; Paillard, V. Photoluminescence Properties of Silicon Nanocrystals as a Function of their Size. *Phys. Rev. B* **2000**, *62*, 15942−15951.
(51) Murphy, C. J.; Coffer, J. L. Quantum Dots: A Primer. *Appl. Spectrosc.* **2002**, *56*, 16A−27A.
(52) Reboredo, F. A.; Franceschetti, A.; Zunger, A. Dark Excitons due to Direct Coulomb Interactions in Silicon Quantum Dots. *Phys. Rev. B* **2000**, *61*, 13073−13087.
(53) Song, D.; Cho, E.-C.; Cho, Y.-H.; Conibeer, G.; Huang, Y.; Huang, S.; Green, M. A. Evolution of Si (and SiC) Nanocrystal Precipitation in SiC Matrix. *Thin Solid Films* **2008**, *516*, 3824−3830.
(54) Cullity, B.; Stock, S. *Elements of X-Ray Diffraction*; 3rd ed., Prentice-Hall Inc.: New Jersey, 2001.
(55) Lopez, T.; Mangolini, L. Low Activation Energy for the Crystallization of Amorphous Silicon Nanoparticles. *Nanoscale* **2014**, *6*, 1286−1294.
(56) Richter, H.; Wang, Z.; Ley, L. The One Phonon Raman Spectrum in Microcrystalline Silicon. *Solid State Commun.* **1981**, *39*, 625−629.
(57) Hessel, C. M.; Wei, J.; Reid, D.; Fujii, H.; Downer, M. C.; Korgel, B. A. Raman Spectroscopy of Oxide-Embedded and Ligand-Stabilized Silicon Nanocrystals. *J. Phys. Chem. Lett.* **2012**, *3*, 1089−1093.
(58) Faraci, G.; Gibilisco, S.; Russo, P.; Pennisi, A. R.; La Rosa, S. Modified Raman Confinement Model for Si Nanocrystals. *Phys. Rev. B* **2006**, *73*, 033307.
(59) Casari, C.; Li Bassi, A.; Baserga, A.; Ravagnan, L.; Piseri, P.; Lenardi, C.; Tommasini, M.; Milani, A.; Fazzi, D.; Bottani, C.; Milani, P. Low-frequency Modes in the Raman Spectrum of sp-sp2 Nanostructured Carbon. *Phys. Rev. B* **2008**, *77*, 195444.
(60) Ferrari, A.; Robertson, J. Interpretation of Raman Spectra of Disordered and Amorphous Carbon. *Phys. Rev. B* **2000**, *61*, 14095−14107.
(61) Casiraghi, C.; Ferrari, A.; Robertson, J. Raman Spectroscopy of Hydrogenated Amorphous Carbons. *Phys. Rev. B* **2005**, *72*, 085401−1−14.
(62) Briggs, D.; Seah, P. *Practical Surface Analysis: Auger and X-ray Photoelectron Spectroscopy; Practical Surface Analysis*; Practical Surface Analysis; John Wiley and Sons: Chichester, 1990.
(63) Salimian, S.; Delfino, M. Removal of Native Silicon Oxide with Low-Energy Argon Ions. *J. Appl. Phys.* **1991**, *70*, 3970−3972.
(64) Grehk, T.; Johansson, L.; Gray, S.; Johansson, M.; Flodstrom, A. Absorption of Li on the Si(100)2 × 1 Surface Studied with High-resolution Core-Level Spectroscopy. *Phys. Rev. B* **1995**, *52*, 16593−16601.
(65) Delplancke, M. P. Preparation and Characterization of Amorphous SiC:H thin films. *J. Vac. Sci. Technol. A* **1991**, *9*, 450−455.
(66) Muehlhoff, L.; Choyke, W. J.; Bozack, M. J.; Yates, J. T. Comparative Electron Spectroscopic Studies of Surface Segregation on SiC(0001) and SiC(000$\bar{1}$). *J. Appl. Phys.* **1986**, *60*, 2842−2853..
(67) Hollinger, G. Structures Chimique et Electronique de l'interface SiO_2—Si. *Appl. Surf. Sci.* **1981**, *8*, 318−336.

(68) Aarnink, W. A. M.; Weishaupt, A.; van Silfhout, A. Angle-resolved X-ray Photoelectron Spectroscopy (ARXPS) and a Modified Levenberg-Marquardt Fit Procedure: A New Combination for Modeling Thin Layers. *Appl. Surf. Sci.* **1990**, *45*, 37−48.
(69) O'Hare, L.-A.; Parbhoo, B.; Leadley, S. R. Development of a Methodology for XPS Curve-fitting of the Si 2p Core Level of Siloxane Materials. *Surf. Interface Anal.* **2004**, *36*, 1427−1434.
(70) Kasavajjula, U.; Wang, C.; Appleby, A. J. Nano- and Bulk-Silicon-based Insertion Anodes for Lithium-Ion Secondary Cells. *J. Power Sources* **2007**, *163*, 1003−1039.